Multilayer, Dynamic, Mixed Solid/Liquid Human Head Models for the Evaluation of Near Infrared Spectroscopy Systems

Meltem Izzetoglu, Juan Du, Kurtulus Izzetoglu, Hasan Ayaz, *Senior Member, IEEE*, Banu Onaral, *Fellow, IEEE*, and Baruch Ben Dor

***Abstract*— Human head-mimicking laboratory models (phantoms) play an essential role in the calibration, testing, and evaluation of near infrared spectroscopy (NIRS)-based optical brain imaging systems. Phantoms reported in the literature are generally of solid nature mimicking the optical properties of the overall human head with just a single layer. Solid phantoms can further be constructed as multilayered to mimic superficial layers of the head or with disks to mimic lesions within the brain layer. However, solid phantoms are of static nature, and hence, changing characteristics within the brain layer, such as in oxygen saturation cannot be modeled. Liquid phantoms can be used to model dynamic changes within the brain; however, existing liquid phantoms are usually of one layer and cannot mimic all the superficial layers of the head. In this article, we report the design and development of a six-layer human head-mimicking phantom that is a mixture of solid compartments modeling the superficial layers of the head and a liquid section mimicking the brain layer which provides a realistic and dynamic design. We also discuss studies which utilized this hybrid, six-layer phantom for the design and evaluation of a NIRS-based brain monitoring system, the hand-held hematoma detector. The results presented here highlight how the proposed phantom approach can be used to assess repeatability/reproducibility, as well as design and execution of agreement tests within and across different models of a NIRS-based brain monitoring device. Our new solid–liquid hybrid phantom model can guide the design and calibration of new NIRS systems, evaluation of their processing algorithms, and testing of the device capabilities under various conditions.**

***Index Terms*— Hematoma detection, near infrared spectroscopy (NIRS), optical head models, solid and liquid tissue phantoms.**

I. Introduction

As NEAR infrared spectroscopy (NIRS)-based optical brain imaging systems gain more widespread use in various applications involving clinical and healthy populations, calibration, testing, characterization, and validation of the design, algorithms and measurements become essential. Human head-mimicking laboratory models (phantoms) have been an integral, necessary, and important part in those processes such as initial or standard system quality tests, characterization of signal-to-noise ratio, or performance comparisons among systems or algorithms [1], [2]. While digital phantoms generated in silico through Monte Carlo (MC) simulations can provide information on light-tissue interaction under various system and tissue parameters in general [3]–[7], physical phantoms can provide in-depth information on the performance of the actual NIRS system. They enable research engineers and optical system designers to build dependable, repeatable, and controlled conditions that can be spatially, temporally, and optically mimicked.

A. Background on Existing Phantoms in the Literature

A wide range of materials and methods exist in the literature for the construction of physical phantoms which basically depends on the structure of the phantom tailored to the application purposes. Typically, there are two types of phantom structures; solid or liquid forms that have been used in the literature [8]–[38]. In solid or liquid phantoms, a base mixture is usually prepared with appropriate amounts of a scattering and an absorbing compound to obtain a laboratory model of the intended head tissue, mimicking its optical characteristics (reduced scattering, μ_s', and absorption coefficients, μ_a [1]–[38]).

A number of material choices are available to produce solid phantoms. For example, agar, gelatin, silicone, and epoxy resins are commonly used as the base substrate or matrix material that can be cured to solidify [8]–[16]. Typically, absorbing dyes of different colors such as carbon black or India ink and scattering agents such as titanium dioxide (TiO_2), aluminum oxide (Al_2O_3), or microspheres are added prior to curing to obtain appropriate absorption and scattering coefficients of the tissue medium to be mimicked. Recently, 3-D printing and rapid prototyping technologies have also been proposed for optical phantom fabrication, where different shapes with curvatures can be modeled [17], [18]. There also exist commercially available solid phantoms built with known absorption and scattering coefficients that researchers can use for the calibration and evaluation of their NIRS systems such as the ones provided by ISS, Inc., or fNIR Devices, LLC.

Manuscript received July 12, 2019; revised April 1, 2020; accepted April 5, 2020. Date of publication April 24, 2020; date of current version September 15, 2020. This work was supported in part by the U.S. Marine Corps under Contract W911QY-10-C-0136 and in part by the Coulter-Drexel Translational Research Partnership Program under Grant 282812-3850. The Associate Editor coordinating the review process was George Xiao. *(Corresponding author: Meltem Izzetoglu.)*

Meltem Izzetoglu is with the Electrical and Computer Engineering Department, Villanova University, Villanova, PA 19085 USA (e-mail: mizzetog@villanova.edu).

Juan Du, Kurtulus Izzetoglu, Hasan Ayaz, and Banu Onaral are with the School of Biomedical Engineering, Science and Health Systems, Drexel University, Philadelphia, PA 19104 USA.

Baruch Ben Dor is with Infrascan Inc., Philadelphia, PA 19104 USA.

Color versions of one or more of the figures in this article are available online at http://ieeexplore.ieee.org.

Digital Object Identifier 10.1109/TIM.2020.2990261

Solid phantoms are generally built as a homogeneous single layer, mimicking the overall optical properties of the underlying tissue, such as the overall human head or only the brain layer. However, the underlying tissue that is intended to be monitored by a NIRS device is generally not homogeneous. There are either various layers of different types of tissues, e.g., the head is formed with skin, scalp, skull, cerebrospinal fluid (CSF), and brain layers or it may have heterogeneity related to disease conditions such as hematoma or tumor development. In order to reach more realistic phantoms, multilayered solid phantoms can be built by using molding-casting methods [19]–[22] either by casting solid phantoms of different thicknesses layer after layer separately and stacking them on top of each other or pouring and solidifying the solid layers on top of each other within the mold itself [16], [22], [23]. Targets with different optical characteristics can also be placed in select layers of different thicknesses during the fabrication process of the solid phantoms to mimic clinical lesions [16], [19], [24]–[26].

If the goal is to test the dynamic changes in terms of absorption or scattering properties for the evaluation of the NIRS system or algorithms, liquid phantoms will be required. Such phantoms can be modeled by using liquid type matrix materials such as lipid emulsion (Intralipid) or milk mixed with water or saline at appropriate percentages to obtain the scattering base in which different types and concentrations of absorbing materials such as ink or erythrocytes, whole blood or hemoglobin can be added [27]–[35]. If dynamic changes in different forms of hemoglobin (oxygenated or deoxygenated) measurements for oxygen saturation assessment are required, hemoglobin becomes the choice of the absorber in liquid phantoms in which case saline should be used in the mixture instead of distilled water to avoid lysing of blood cells. In such applications, hemoglobin content can be oxygenated by delivering oxygen to the mixture from an oxygen tank and deoxygenation can be induced by adding yeast to the liquid phantom. It was shown that liquid phantoms can be used for several hours or days preserving its optical characteristics, but eventually, they have to be discarded in an appropriate fashion since the materials used will either go bad or lose their optical stability [30].

There have been some studies in the literature to build multilayer liquid phantoms such as reported by Gagnon *et al.* [36] and Gibson *et al.* [37]. In both of these studies, the head was mimicked with only two layers formed by the outer layer mimicking skin/scalp, skull, and CSF altogether and the inner layer for the brain. In Gagnon *et al.* [36], the phantom was a cubic container made up of acrylic glass which can model the overall head as a homogeneous one layer by filling it with an intralipid mixture. The container can also be divided via a thin plastic membrane into two layers. The outer layer can be filled with an intralipid solution mimicking the superficial layers of the head (scalp, skull, and CSF) altogether and the inner layer can then be filled with an intralipid and glycerol mixture to introduce realistic flow changes. Even though it was only a two-layer model, the findings suggested that the two-layered model provided a better estimate of the flow change than the homogeneous one-layer model.

In Gibson *et al.* [37], a neonatal head-mimicking phantom was built as a two-layer model, where superficial layers of scalp and skull were of solid nature and the brain layer was formed as a liquid mixture. The solid outer shell was cast using epoxy resin, TiO_2, and dye combination with optical properties of scalp and skull layers in combination in a mold made from an anatomically realistic doll. The phantom was made hollow so that the inner spherical region can be filled with epoxy resin without the hardener to remain liquid and with appropriate scattering and absorbing compounds to mimic the brain. The nature of the liquid mixture of the phantom allowed modeling targets within the brain layer by suspending two epoxy resin cylinders on thin wires within the upside-down phantom which was aimed to be resolved. Authors had mentioned that this phantom was a simplification of a real neonatal head where nonscattering regions such as CSF were not simulated. In another former study by Del Bianco *et al.* [38], a fully liquid multilayer phantom was proposed where different head layers were mimicked by compartments in a container filled with liquid mixtures of different absorption and scattering characteristics that are separated by thin membranes. Their experiments showed that for the separator membrane, a material with appropriate scattering properties should be used to avoid perturbation in the measurements and Mylar film was proposed as a suitable choice, even though it caused perturbation in continuous-wave system measurements up to 8%.

B. Motivation

Although solid phantoms are sturdy, portable, durable, and even can be produced to have different layers or lesions, the model is "fixed" and cannot be varied to determine the effects of dynamic changes or perturbations in different layers, such as oxygenation of hemoglobin or melanin content. On the other hand, despite the fact that, liquid phantoms provide dynamic changes in the tissue medium effectively, they are still designed mostly as one layer, built in a container and cannot mimic multilayered tissue mediums. The existing multilayer liquid phantoms are not completely realistic models of the human head, not having all anatomical layers or can generate additional scattering or reflection problems with the use of separate membranes.

C. Current Study

In this article, our approach was to address the challenges and limitations of existing head-mimicking phantoms such as having a solid nature and not allowing dynamic changes within the brain layer or being of liquid nature and not modeling all of the superficial head layers. The proposed phantom models the human head realistically with all its layers of skin, scalp, skull, CSF, and brain with their corresponding optical properties and thicknesses. In addition, our model allows dynamic changes within the brain so that oxygenation and deoxygenation or clinical conditions such as hematoma or edema development of different sizes and depths can be modeled. This new design is a multilayered mixed solid and liquid phantom, where multilayer solid phantoms using silicone, TiO_2, and dye combinations are built on top of each other in a sequential manner. A molding

and casting procedure is used in a certain order so that a cubic container having various layers of different thicknesses in its walls mimicking the superficial head layers can be generated. Furthermore, within the middle compartment of the cubic container brain tissue can be dynamically modeled with a liquid phantom structure where NIRS measurements can be obtained from the outer side of the phantom walls.

We used this realistic and versatile multilayered mixed solid/liquid phantom in the testing and evaluation of NIRS-based brain imaging system designs or analysis algorithms [39]–[41]. Here, we report on one of these studies where we have used the proposed phantom on the performance comparison (equivalence test) of two models of a NIRS-based hand-held hematoma detector, namely Infrascanner produced by InfraScan, Inc. [42]–[45]. Repeatability, reproducibility, and agreement in the measurements performed by different units of the same scanner model and between scanner models were compared under hematomas of different sizes and depths and for different skin color conditions.

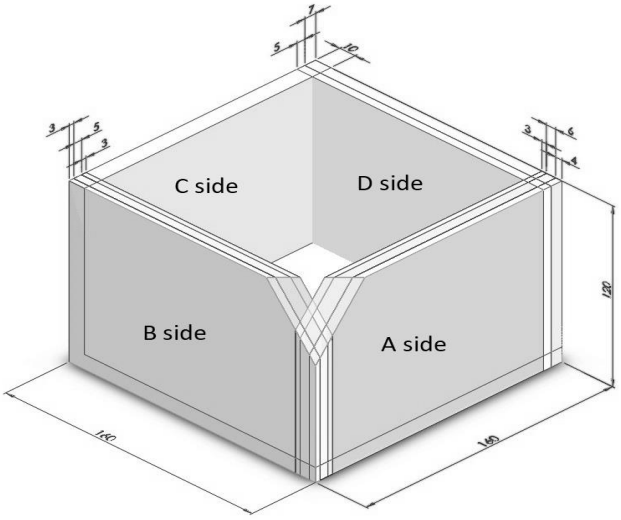

Fig. 1. Schematic of the multilayer mixed liquid and solid optical head phantom. All dimensions are given in mm.

II. Multilayer Mixed Solid and Liquid Dynamic Phantom Design and Development

A. General Structure of the Phantom

The solid base of the mixed phantom was cubic shaped where the top side was left open to allow filling the empty compartment in the middle of the phantom with an appropriate liquid phantom solution to mimic dynamic changes in the brain layer of the human head. Each of the four sides of the mixed phantom could be configured to have a varying number of wall layers with different optical properties and thicknesses to mimic the physical and optical properties of human head layers. The sides, namely A, B, C, and D, are shown in Fig. 1. In this article, we have selected to build our phantom where A and B sides (thick and thin side, respectively) have three layers of the human head composed of scalp, skull, and CSF with differing properties, C side has just one layer with clear optical properties such as water, and D side has two layers of scalp and skull with differing properties. In addition, thin neutral density (ND) Wratten 2 film filters by Kodak [46] could be placed over the scalp layer of the phantom to mimic the epidermis layer of different skin colors. Note that the thickness of the film filters (0.1 mm) is similar to the thickness of human skin. The bottom side was made up of one piece of polyethylene which was shaped by a modular molding casting method.

B. Materials and Methods Used to Form Multilayered Sides in the Solid Base of the Phantom Walls

1) Materials Used: The room temperature vulcanizing (RTV) 12 silicone material was selected to make a multilayered solid phantom since silicone matches the mechanical and optical properties of the tissue more closely. RTV 12 silicone product (GE Silicones) consists of two parts: RTV 12A (base compound) and RTV 12C (curing agent). RTV 12A is 80% polydimethylsiloxane, 10% MQ resin, benzene, and toluene. RTV 12C is 5% dibutyl tin oxide solution, 20% ethyl silicate 40, 20% aminopropyltriethoxysilane, 5% 1,2,4-trimethylbenzene and naphtha (mineral spirits 60%). The weight ratio of 20:1 of RTV 12A:RTV 12C was recommended by the manufacturer. The recommended curing time was 72 h. However, 24 h is usually enough to solidify the liquid phantom mixture. In order to achieve certain absorbing and scattering properties to mimic different layers of the head tissue other compounds were added to the RTV 12 before curing it. The carbon black (Raven 5000 Ultra II, Columbian Chemistry Company) was used as the absorbing agent where the mean particle size of the carbon black was around 8 nm. For the scattering agent, TiO_2 from Sigma (T-8141) was used.

2) Sequential Molding Casting Process to Form Each Multilayered Solid Phantom Wall: Cast molding is the technique generally used to make solid phantoms of various layers since it does not need too much strength to put pressure to make and combine the layers. In addition, the equipment can be of any size, shape, and weight, and the tools needed are easy to find and construct. Hence, we used the cast molding technique to construct each side of the multilayer solid head phantom walls.

The making process of solid phantom walls of select layers involved the following procedures in order.

1) Prepare the liquid mixture of different ratios of carbon black and TiO_2 within the RTV 12 solution made up of RTV 12A and RTV 12C mimicking optical properties (μ_a and μ_s') of the selected extracerebral head tissue layers at specific wavelengths of light using the method described by Bays *et al.* [47] and Beck *et al.* [48].
2) Verify the optical properties of the prepared phantom layer mixture by testing it via another optical measurement system, namely the in-phase and quadrature-phase (IQ) system, based on the frequency domain technique [49].
3) Pour the appropriate volume of the prepared silicone mixture into the mold of the known base area to obtain a select thickness of the outer head layer of the phantom wall. The mold we had in our laboratory was cubic

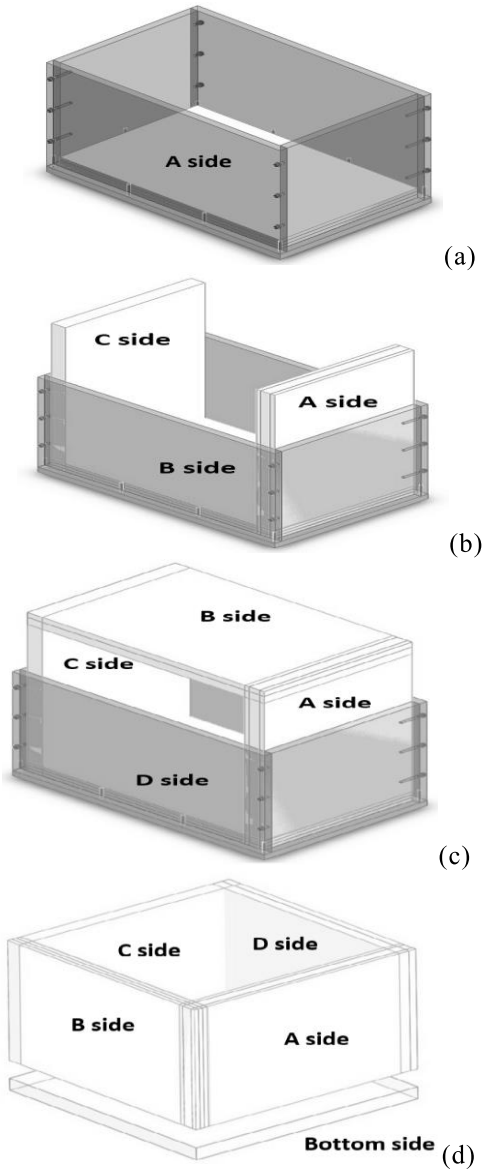

Fig. 2. Sequential molding casting process. (a) Three layers of skin, skull, and CSF were casted by pouring silicone mixture into the mold layer by layer for the A and C sides of the phantom, separately. (b) A and C sides linked together during the forming of B side. (c) A, B, C, and D sides linked together during the forming of D side. (d) All four sides are linked together by the bottom side forming the cubic container.

shaped (160 mm × 160 mm × 120 mm) with only the top side open allowing pouring of the liquid mixture of necessary volume to generate the required width, length, and height of each side of the solid phantom walls as shown in Fig. 2(a).

4) Wait the curing time of at least 24 h for the first layer of the phantom wall to solidify.
5) Repeat the procedure from 1)–4) to form select head tissue layers on top of each other starting from the outer extra-cerebral layer till the inner one until the brain layer, forming one wall of the solid phantom base having multilayered structure at the end of the process.

3) Sequential Molding Casting Process to Form Overall Phantom Structure: The sides of the phantom were also produced sequentially in such a way that during their molding they were also connected to each other as follows.

1) Form the A- and C-side walls as multilayered solid phantom blocks of select head layers with chosen optical properties and thicknesses of interest, separately in the bottom of the mold [see Fig. 2(a)] using the cast molding technique described in Section II-B2.
2) Place the previously and separately formed A- and C-side solid phantom blocks on opposite walls of the mold, and form the B-side of the phantom layer by layer using the process as given in Section II-B2 so that while the multilayered B side was cured at the bottom of the mold, A, B, and C sides were linked and connected together at their corners as shown in Fig. 2(b).
3) Flip the already formed and connected solid phantom with sides A, B, and C and place it in the mold in such a way that B side was on the open, top side of the mold and the A and C sides are touching the opposite walls of the mold where their open ends are touching the bottom of the mold as shown in Fig. 2(c). With this arrangement, form the D-side layer by layer using the process explained in Section II-B2 so that the open ends of A and C sides in the bottom of the mold are linked and connected.
4) Form the bottom side of the phantom using one piece of polyethylene by connecting it to the A, B, C, and D sides with the use of silicone mixture after it is cured as shown in Fig. 2(d).

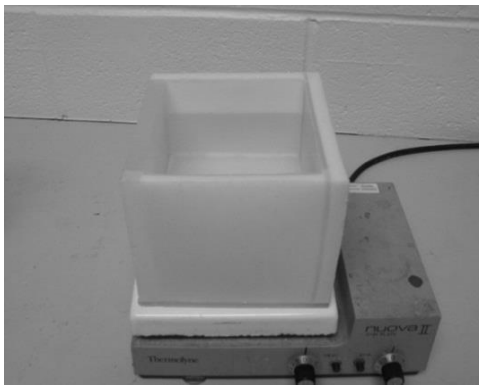

Fig. 3. Actual phantom with solid superficial layers built with molding casting method and liquid and hence, dynamic brain layer.

C. Final Form of the Phantom With Its Select Optical Properties and Thicknesses in Each of Its Multilayered Walls

The multilayer solid base of the head phantom that was designed, developed, and constructed is as shown in Fig. 3.

The thickness of the existing layers on each sidewall of the phantom selected to be developed in this article is presented in Table I. Note that the thickness of extracerebral tissue layers greatly varies individually and with age, gender, ethnicity, and head locations [50]–[52]. Here, we adopted commonly used scalp, skull, and CSF thicknesses in the literature on A and B sides of the phantom [16], [50]. We adjusted the thickness of the layers used in C and D sides so that the total thickness

TABLE I
THICKNESS OF HEAD PHANTOM LAYERS ON EACH SIDE (IN mm)

Sides	Scalp	Skull	CSF
A	4	6	3
B	3	5	3
C	-	-	13
D	5	7	-

TABLE II
OPTICAL PROPERTIES OF VARIOUS LAYERS ON EACH SIDE OF THE PHANTOM MEASURED AT 810-nm WAVELENGTH

	Scalp		Skull	
Sides	μ_a (cm^{-1})	μ_s' (cm^{-1})	μ_a (cm^{-1})	μ_s' (cm^{-1})
A	0.1043	12.49	0.0891	12.12
B	0.0873	10.86	0.081	12.98
C	-	-	-	-
D	0.0934	11.89	0.0716	12.62

adds up to regular extracerebral layer thickness of the adult human head of 11–13 mm.

The corresponding optical properties of the solid phantom wall layers mimicking the extracerebral tissues are summarized in Table II. Note that here we present the absorption and reduced scattering coefficients measured by the frequency domain IQ system at 810-nm wavelength only, since it is the same wavelength used in Infrascanner even though we have other wavelength measurements, also. The optical parameters were measured during the sequential making process of the layers and walls, hence, the slight differences in them for the same head layer type at different sides.

In all the sides where CSF was present, it was formed by the RTV 12 solution without the addition of carbon black and TiO_2, since it is a clear layer, to mimic optical properties similar to water. Hence, on each side of the phantom, the absorption coefficient ($\mu_a = 0.0365$ cm^{-1}) and reduced scattering coefficient ($\mu_s' = 1.02$ cm^{-1}) of the CSF layer were small and close to optical properties of water and in line with the previously published and used ranges [7], [36], [53]. The absorption and scattering parameters and thicknesses of the layers on the A side were selected to mimic a less transparent tissue, i.e., with darker and thicker skin, whereas B side is selected to mimic a more transparent head tissue (light and thinner skin, and so on). The single clear layer on the C side without any other superficial layers and the two-layered D side without the effects of the CSF layer were designed to allow comparisons on the measurements that can be collected simultaneously from the A and B sides.

Note that different sides of the phantom were designed in a certain way in the current development of the phantom to mimic adult head with and without various superficial layers as explained here. However, using the methodology explained, any kind of mixed phantom with desired optical properties and thicknesses in its layers can be built for example to mimic different age groups, ethnicities, and head locations. The flexibility of the phantom lies not only in its multilayer solid base mimicking superficial head layers but also in its liquid nature within the brain layer allowing dynamic measurements. The dynamic changes within the brain layer can be obtained by filling the open compartment in the middle of the phantom with a liquid mixture of changing optical properties (by oxygenating or deoxygenating a blood-based liquid). Moreover, hematoma or edema models (blood or water-filled latex balls) can be inserted in the brain layer from the open to side of the phantom. Such studies conducted using this phantom will be explained in Section III that utilized this realistic and flexible way of modeling various healthy and clinical conditions in the human head for the testing and evaluation of NIRS-based brain imaging devices.

III. TESTS PERFORMED USING MULTILAYER MIXED SOLID AND LIQUID PHANTOM

A. Motivation

NIRS-based instruments can go through various model upgrades over time due to user, environmental, or technical needs. As each model gets designed and developed, the new model is usually compared with the earlier version for their substantial equivalence to show that the new version is at least as safe and effective as the predicate, the older version. Such equivalence tests can be efficiently performed through appropriate phantom models. Here, we present the results of such equivalence tests between the two models of a NIRS-based brain imager, namely Infrascanner by InfraScan, Inc. that employed the multilayered solid and liquid phantom as its testbed.

B. Methodology

1) Equipment: Infrascanner is a hand-held, U.S. Food and Drug Administration (FDA) cleared, NIRS-based brain hematoma detector which can be timely and effectively used in the field and as a triaging tool for computed tomography (CT) scanning during an event of head trauma [54]. The device compares light attenuation or optical density (OD) on two contralateral sides of the head in its decision process for hematoma detection. If the difference in OD on contralateral sides of the head (ΔOD) is less than the detection threshold (τ) of 0.2, then the device results in a no hematoma outcome, otherwise its result will be a hematoma present. Hence, the condition on Infrascanner outcome for hematoma present is

$$\Delta \mathrm{OD} = \log_{10}\left(\frac{I_\mathrm{N}}{I_\mathrm{H}}\right) \geq \tau \tag{1}$$

where the detection threshold, $\tau = 0.2$, I_N is the intensity of reflected light on the normal side, and I_H is the intensity of reflected light on the hematoma side of the head.

The tests explained here were conducted to show the substantial equivalence of Infrascanner model 2000, the newer version at the time of comparison to the older version model 1000. The tests as explained here were used in the FDA application of model 2000.

2) Phantom Model and Test Setup: Previously described multilayered mixed solid and liquid optical phantom mimicking human head in Section II was used in all these tests that will be explained here. Measurements using the two

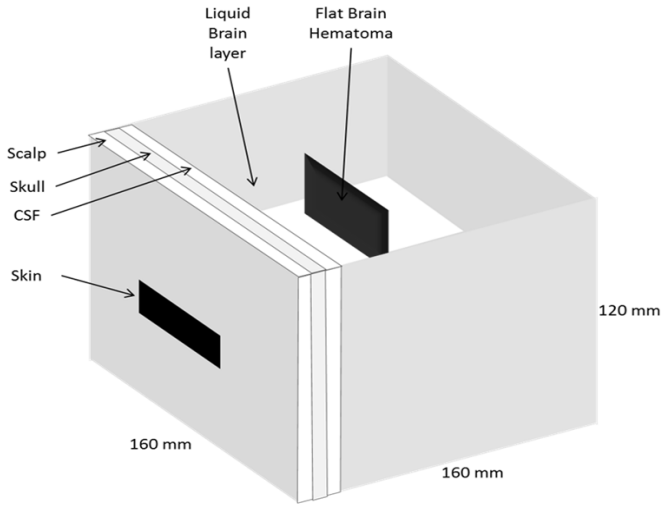

Fig. 4. Schematic of the six-layer phantom model, where superficial head layers of skin, scalp, skull, CSF, and brain with and without hematoma were modeled.

Infrascanner models were collected from the skin surface of the B-side of the phantom with layer characteristics as given in Tables I and II. The brain tissue was formed in the middle container of the phantom, as a liquid layer prepared as a combination of water, Intralipid (20% fat emulsion) as the scattering compound and India ink (Speedball, super black, India ink) as the absorbing compound of certain concentrations to create a simulation of brain tissue with $\mu_a = 0.1\ \text{cm}^{-1}$ and $\mu_s' = 5\ \text{cm}^{-1}$ in line with prior published values [16], [55].

Since the brain layer of this multilayer phantom was of liquid nature, hematomas of different size and depth could be modeled. Our approach was to use whole animal (sheep) blood as hematoma. Following FDA guidance, a flat hematoma model was used in this test which was built using a black color painted wooden rectangular frame, inserted into a latex ball, and filled with blood. The rectangular frame forced the shape of the hematoma to remain relatively flat. For each hematoma size, a dedicated frame of certain length, width, and thickness was generated so that certain volume of hematoma (3, 5, 10, 30, and 50 cc) could be obtained.

Thin ND Wratten 2 film filters by Kodak were placed over the phantom to adjust the signal levels in Infrascanner measurements to OD values observed in former clinical studies mimicking patients with different skin colors. Using those filters, the OD values in the laboratory tests covered the range of 5–5.8 OD to simulate light-skinned patients and 6.3–7.1 OD to simulate dark-skinned ones similar to the OD values obtained from actual patients. The thickness of the film filters (0.1 mm) was similar to the thickness of the human skin. With the described configuration as a result, including the four solid layers of skin, scalp, skull, and CSF together with the liquid brain layer and a bag with sheep blood to simulate brain hematoma, six-layer model was developed as shown in Fig. 4, which was also requested and agreed by the FDA in Infrascanner testing.

The overall test setup used to collect and compare data from two models of Infrascanner in this article was shown in Fig. 5. The phantom was positioned within a dedicated

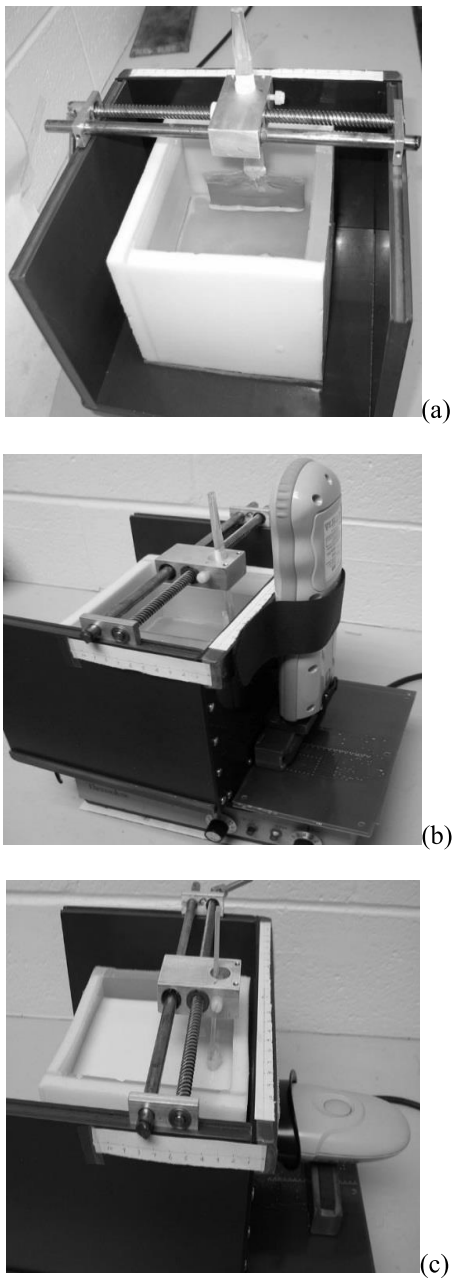

Fig. 5. Multilayer solid and liquid phantom with brain hematoma model positioned within a dedicated frame to support the sensors and the hematoma model fastened to a sliding rail (a). Infrascanner models 2000 and 1000 positioned during laboratory tests (b) and (c), respectively.

frame to support the sensors, and the hematoma model which can be built of different sizes was fastened to a sliding rail for support and to be able to change its depth from the surface (at 0, 1, 2, and 3 cm below CSF) in a controlled fashion as shown in Fig. 5.

C. Comparison Tests and Statistical Analysis

In order to demonstrate substantial equivalence between Infrascanner model 1000 and model 2000, we have performed two tests as explained below.

1) Test 1 (Repeatability/Reproducibility Test): The repeatability and reproducibility test data involved repeated

observations with four different systems for each of the two scanner models (four systems of model 1000 and four systems of model 2000). Hematoma models of 5 and 50 cc were evaluated at depths of 0, 1, 2, and 3 cm within the multilayer mixed solid and liquid phantom setup as explained above. In order to provide a comparison for the calculation of ΔOD values, the hematoma model was also removed from the phantom for a baseline OD estimate (no hematoma condition). Each measurement condition was repeated by each device 40 times to provide 80% power.

The proportion of variance explained by the hematoma size, depth, system, and repeated observations (within-system and between-system variability) over the total variance (TV) was estimated. This was done separately for scanner models 1000 and 2000 results, separately and provided as a descriptive investigation.

An analysis of variance (ANOVA) was performed that modeled the ΔOD as a function of hematoma size, depth, and machine. Estimates for ΔOD values were obtained by finding the difference between the mean OD values obtained for hematomas at a given depth and the mean OD values with the model hematoma removed from the tank for the matching system. The estimated ΔOD means were compared between scanner models by hematoma size and depth where the mean difference and the standard error (SE) were also calculated [56].

2) Test 2 (Agreement Test): The agreement test data were collected using one system of each scanner model (one system of model 1000 and one system of model 2000) for hematomas of size 5, 10, and 50 cc at different depths 0, 1, and 2 cm and for two skin types (light and dark skin color). The measurements were also obtained without a model hematoma in the phantom. Each measurement condition was repeated 40 times.

Mean ΔOD values were estimated by subtracting the results with the hematoma out of the phantom from the results with the hematoma in the phantom. An ANOVA was performed that modeled ΔOD as a function of hematoma size, depth, skin type, and model. The estimated mean ΔOD values were calculated by hematoma size, depth, and model. The difference in ΔOD values between the scanner models and the SE were compared overall, by hematoma size, depth, and skin type, and by hematoma size and skin type.

IV. Results

A. Test 1: Results for Repeatability/Reproducibility

Across the two hematoma models and four depths, the mean OD values ranged from 5.05 to 5.78. The variance and standard deviation (SD) in OD were estimated across all of the observations in order to obtain between-system and within-system variance estimates which were found to constitute a very small percentage of the overall variance in the data for both scanner models. Note that, in Table III, percent of the total variance (%TV) for each source was calculated first by finding the TV which is the sum of all variances, σ_k^2 from each of the provided sources in Table III (2) and then using it in the formula given in (3) as follows:

$$\mathrm{TV} = \sum_{k=1}^{5} \sigma_k^2 \tag{2}$$

$$\%\mathrm{TV}_k = \frac{\sigma_k^2}{\mathrm{TV}}, \quad k = 1, 2, \ldots, 5. \tag{3}$$

Hence, Table III indicates the percent of TV across the samples that could be attributed to the various sources. The overall variance was nearly identical across the two scanner models including the variances between systems and within systems.

We have also compared ΔOD values between scanner models by averaging across the four systems within each model of the scanner. Table IV compares the average ΔOD for scanner models by hematoma size and depth using an ANOVA model. None of the estimated differences are statistically significant (probability value, p, is greater than the selected significance value of 0.05) and all of the differences between the two model measurements and SE were very small.

In summary, the repeatability and reproducibility test data indicate that both scanner models behave nearly identically and have a high degree of precision as expressed by low SD and SE values.

TABLE III

Estimated TV of OD Measurements for the Reproducibility and Precision Test Data by Scanner Model

Model	Source	Variance, σ^2	*%TV*	SD
1000	1. Hematoma Size	0.00806	8.5%	0.090
	2. Depth	0.05446	57.7%	0.233
	3. Size x Depth	0.03134	33.2%	0.177
	4. Between Systems	0.00017	0.2%	0.013
	5. Within System	0.00028	0.3%	0.017
	Total	0.09432		0.307
2000	1. Hematoma Size	0.00786	8.3%	0.089
	2. Depth	0.05445	57.8%	0.233
	3. Size x Depth	0.03139	33.3%	0.177
	4. Between Systems	0.00016	0.2%	0.013
	5. Within System	0.00030	0.3%	0.017
	Total	0.09416		0.307

TABLE IV

Scanner Model Comparison of Estimated ΔOD by Hematoma Size and Depth for the Reproducibility and Precision Test

Hematoma Size (cc)	Depth (cm)	ΔOD Estimate		Difference (SE)	P-value
		Model 1000	Model 2000		
5	0	0.477	0.472	-0.005 (0.0054)	0.3733
	1	0.242	0.248	0.006 (0.0054)	0.2957
	2	0.120	0.128	0.008 (0.0054)	0.1517
	3	0.044	0.046	0.002 (0.0054)	0.7228
50	0	0.687	0.692	0.005 (0.0054)	0.3515
	1	0.380	0.380	0.000 (0.0054)	0.9954
	2	0.224	0.225	0.001 (0.0054)	0.8855
	3	0.102	0.104	0.002 (0.0054)	0.7030

B. Test 2: Results for Agreement

Plots for ΔOD values for different hematoma sizes at different depths and skin colors are presented in Fig. 6. Even though skin color affected ΔOD value (lower in dark skin as compared to light, as expected), the difference between the

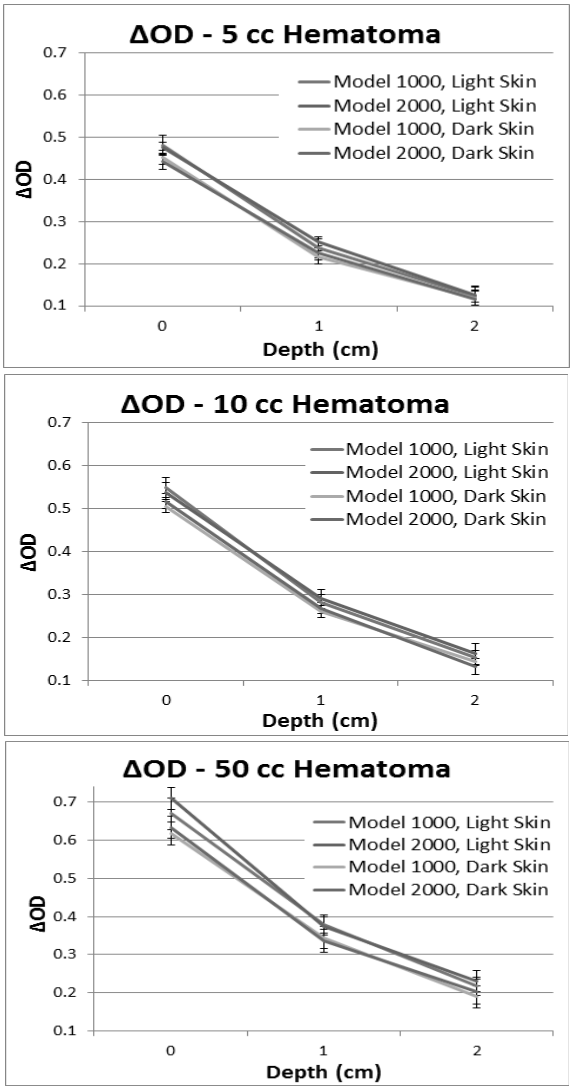

Fig. 6. Average ΔOD values (±SD in error bars) for hematomas of size (a) 5 cc, (b) 10 cc, and (c) 50 cc at depths 0, 1, and 2 cm for light and dark skin color as measured by scanner models 1000 and 2000.

two model measurements was very small in each skin color type.

In an ANOVA model comparison of the overall mean ΔOD averaged across all hematoma sizes and depths separately for light and dark skin, the scanner model 1000 ΔOD was 0.344 for light skin and 0.316 for dark skin and the scanner model 2000 ΔODs were 0.351 and 0.319, respectively, where both light and dark skin ΔODs were not significantly different from each other ($p = 0.1760$ and 0.6073, respectively) between scanner models. Similarly, as shown in Table V, the average ΔODs by depth and hematoma size were mostly not significantly different. Some small differences in the two Infrascanner models ΔODs reached statistical significance when comparing the scanner models by hematoma size and depth. However, these small differences are not considered to have clinical significance as will be explained in the Section V. Furthermore, as can be noted, the differences in ΔOD are not consistently in the direction of either scanner model.

TABLE V
COMPARISON OF ESTIMATED ΔOD VALUES OF SCANNER MODEL 1000 AND SCANNER MODEL 2000 BY HEMATOMA SIZE, DEPTH, AND SKIN TYPE

Hematoma Size (cc)	Depth (cm)	Skin Color	Estimated Mean ΔOD		Difference (SE)	P-value
			Model 1000	Model 2000		
Overall	Overall	Light	0.344	0.351	0.007 (0.0054)	0.1760
		Dark	0.316	0.319	0.003 (0.0054)	0.6073
Overall	0	Light	0.567	0.575	0.008 (0.0054)	0.1436
		Dark	0.525	0.531	0.006 (0.0054)	0.3053
	1	Light	0.300	0.305	0.006 (0.0054)	0.2945
		Dark	0.273	0.277	0.004 (0.0054)	0.4953
	2	Light	0.164	0.173	0.008 (0.0054)	0.1214
		Dark	0.150	0.149	-0.001 (0.0054)	0.8686
5	Overall	Light	0.280	0.284	0.004 (0.0054)	0.4645
		Dark	0.262	0.261	-0.001 (0.0054)	0.8808
	0	Light	0.481	0.475	-0.005 (0.0054)	0.3369
		Dark	0.451	0.442	-0.010 (0.0054)	0.0663
	1	Light	0.237	0.251	0.014 (0.0054)	0.0111
		Dark	0.215	0.226	0.011 (0.0054)	0.0361
	2	Light	0.123	0.126	0.003 (0.0054)	0.5403
		Dark	0.118	0.115	-0.004 (0.0054)	0.4778
10	Overall	Light	0.328	0.330	0.002 (0.0054)	0.7163
		Dark	0.303	0.306	0.003 (0.0054)	0.6120
	0	Light	0.549	0.538	-0.011 (0.0054)	0.0353
		Dark	0.506	0.517	0.011 (0.0054)	0.0374
	1	Light	0.282	0.290	0.008 (0.0054)	0.1214
		Dark	0.260	0.268	0.008 (0.0054)	0.1192
	2	Light	0.153	0.162	0.009 (0.0054)	0.0997
		Dark	0.143	0.131	-0.011 (0.0054)	0.0341
50	Overall	Light	0.423	0.439	0.016 (0.0054)	0.0031
		Dark	0.384	0.391	0.006 (0.0054)	0.2363
	0	Light	0.670	0.710	0.040 (0.0054)	<0.0001
		Dark	0.618	0.633	0.015 (0.0054)	0.0047
	1	Light	0.380	0.375	-0.005 (0.0054)	0.3440
		Dark	0.345	0.336	-0.009 (0.0054)	0.1076
	2	Light	0.218	0.230	0.013 (0.0054)	0.0170
		Dark	0.190	0.202	0.013 (0.0054)	0.0197

The differences are small relative to the mean value and achieve significance only at higher ΔOD values. In part, due to the low variance in the repeated measurements and the large sample size, the SE is quite small and hence, the significance is also reflective of having a great deal of statistical power.

Overall, there was an effect of lowering the ΔOD value as a function of skin color, but within each skin color, the ΔOD estimates were similar across the two scanner models. This is also true when averaging over hematoma sizes by depth. However, some significant differences were observed for the larger hematoma sizes though trends were not always in the same direction. The large difference in ΔOD values occurred for the 50 cc hematoma at 0 cm depth where the OD values were the largest, and the ΔOD values were well in excess of the threshold, $\tau = 0.2$ as in (1). Since this analysis did not include multiple systems at each level, this may be representative of small system differences that are significant due to the high statistical power. The only assessment that was close to the $\tau = 0.2$ threshold as in (1) was the 50 cc hematoma at 2 cm. Here the scanner model 2000 would have been slightly more sensitive to the presence of a hematoma. Aside from that hematoma size and depth combination, the assessments from both scanner models would have provided a similar ΔOD and hence, a diagnostic answer in both skin types.

In summary, the scanner models performed similarly across a range of hematoma sizes and depths. Both scanner models demonstrated a low degree of variability in repeated measurements across the assessed combinations. Skin color did not

appear to result in a meaningful difference in performance between the scanner models, though dark skin color reduced the ΔOD value for both models by a small amount. The difference in ΔOD values was small relative to the large increase in OD values resulting from the simulated dark skin.

V. Discussion

Extensive laboratory testing of the two Infrascanner models was performed on the multilayer mixed solid and liquid phantom with the brain hematoma model. The multilayer phantom model provided a closer approximation of human tissue, the ΔOD values more closely approximating the signal levels observed in clinical studies [42], [44]. For example, ΔOD values for superficial hematomas were substantially lower in the multilayer model due to the interposition of scalp and bone layers between the sensor and hematoma. In addition, higher scattering in the superficial layers (scalp and bone) contributed to a stronger signal from the deep brain layers, which diminished more slowly with depth. Hence, the results with the multilayer phantom model for both the scanner model 1000 and model 2000 are consistent with the expected results observed in clinical testing of the predicate model 1000, where detection was higher for larger hematomas closer to the surface of the brain and somewhat lower for smaller hematomas at greater distances from the surface. In summary, the phantom model used in this testing provides a robust head model with and without hematoma for the purpose of comparing the performance of the new and legacy Infrascanner models (1000 and 2000, respectively). Furthermore, the phantom tests demonstrate that both system's performances are substantially similar across a range of depths and sizes of hematomas similar to those observed in the clinical setting.

The test data sets suggest that the Infrascanner models are also substantially equivalent for light and dark skin across a range of simulated hematoma sizes and depths. It should be noted that the testing of simulated light and dark skin types covered a range of ODs between 5 and 7, similar to the range observed in the clinical study [42].

Small between system differences were observed in OD values although this was not the case in ΔOD values. Both scanner models had small variances associated with repeated measurements which are not unexpected and were within the device specifications. Because there was some variance between systems it was important to include repeatability testing of multiple systems of each model in order to demonstrate the equivalence. The results indicate that the within-system variability is small and similar for the Infrascanner models 1000 and 2000. The overall variance was nearly identical across the two models of the scanner, including variance between systems and within systems. Note that these differences are in the OD measurements and smaller in calculated ΔOD estimates. The differences and variances are so small that unless ΔOD is almost exactly at the $\tau = 0.2$ threshold cutoff value as in (1), all of the systems tested would lead to the same classification of risk for a hematoma regardless of the Infrascanner model. These small differences would not have clinical significance. Hence, these phantom testing strongly confirms the substantial equivalence of the Infrascanner model 2000 to model 1000.

VI. Conclusion

We introduce here the design and development of a realistic, versatile, and dynamic optical head phantom and its implementation in the testing and evaluation of NIRS systems. The new phantom combines the advantages of solid and liquid phantoms: 1) by modeling a multilayered human head with skin, scalp, skull, and CSF layers of different thicknesses and optical characteristics; and 2) by providing a dynamic brain layer where variations in oxygenation in healthy and clinical conditions of hematoma and edema development or hypoxia can be modeled. Furthermore, the proposed phantom can be designed and developed to model different age groups, head locations, or skin colors. These realistic and versatile phantom designs can guide calibration of NIRS system designs, evaluation of their processing algorithms, and testing of the device capabilities under various conditions. With controlled and repeatable tests that can be performed using these realistic phantoms, the detection limits of a NIRS device and its resolution in discerning different clinical conditions can be reliably and safely investigated. Such findings can further guide animal and human tests for the clinical evaluation of the device and help regulators in the assessment of NIRS-based monitoring systems. Specifically, in applications involving vulnerable populations (e.g., pediatric), realistic phantom tests can be crucial since extreme conditions, such as large hematoma development which can be of low prevalence but holds high risk, can be safely and repeatedly modeled and evaluated.

Acknowledgment

The authors would like to thank Dr. Kambiz Pourrezaei for his valuable discussions.

References

[1] B. W. Pogue and M. S. Patterson, "Review of tissue simulating phantoms for optical spectroscopy, imaging and dosimetry," *J. Biomed. Opt.*, vol. 11, no. 4, 2006, Art. no. 041102.

[2] A. E. Cerussi *et al.*, "Tissue phantoms in multicenter clinical trials for diffuse optical technologies," *Biomed. Opt. Express*, vol. 3, no. 5, pp. 966–971, May 2012.

[3] L. Wang, H. Ayaz, M. Izzetoglu, and B. Onaral, "Evaluation of light detector surface area for functional near infrared spectroscopy," *Comput. Biol. Med.*, vol. 89, pp. 68–75, Oct. 2017.

[4] R. Francis, B. Khan, G. Alexandrakis, J. Florence, and D. MacFarlane, "NIR light propagation in a digital head model for traumatic brain injury (TBI)," *Biomed. Opt. Express*, vol. 6, no. 9, pp. 3256–3267, Sep. 2015.

[5] W. Feng, D. Haishu, T. Fenghua, Z. Jun, X. Qing, and T. Xianwu, "Influence of overlying tissue and probe geometry on the sensitivity of a near-infrared tissue oximeter," *Physiol. Meas.*, vol. 22, no. 1, pp. 201–208, Feb. 2001.

[6] L. Wang, H. Ayaz, and M. Izzetoglu, "Investigation of the source-detector separation in near infrared spectroscopy for healthy and clinical applications," *J. Biophoton.*, vol. 12, no. 11, Jul. 2019, Art. no. e201900175.

[7] E. Okada and D. T. Delpy, "Near-infrared light propagation in an adult head model. II. Effect of superficial tissue thickness on the sensitivity of the near-infrared spectroscopy signal," *Appl. Opt.*, vol. 42, no. 16, pp. 2915–2921, Jun. 2003.

[8] H. J. Juttula, T. P. Kananen, and A. J. Makynen, "Instrument for measurement of optical parameters of turbid media by using diffuse reflectance of laser with oblique incidence angle," *IEEE Trans. Instrum. Meas.*, vol. 63, no. 5, pp. 1301–1309, May 2014.

[9] Y.-P. Huang, Y.-P. Zheng, S.-Z. Wang, Z.-P. Chen, Q.-H. Huang, and Y.-H. He, "An optical coherence tomography (OCT)-based air jet indentation system for measuring the mechanical properties of soft tissues," *Meas. Sci. Technol.*, vol. 20, no. 1, Jan. 2009, Art. no. 015805.

[10] G. Quarto, A. Pifferi, I. Bargigia, A. Farina, R. Cubeddu, and P. Taroni, "Recipes to make organic phantoms for diffusive optical spectroscopy," *Appl. Opt.*, vol. 52, no. 11, pp. 2494–2502, Apr. 2013.

[11] R. Cubeddu, A. Pifferi, P. Taroni, A. Torricelli, and G. Valentini, "A solid tissue phantom for photon migration studies," *Phys. Med. Biol.*, vol. 42, no. 10, pp. 1971–1979, Oct. 1997.

[12] G. J. Greening *et al.*, "Characterization of thin poly(dimethylsiloxane)-based tissue-simulating phantoms with tunable reduced scattering and absorption coefficients at visible and near-infrared wavelengths," *J. Biomed. Opt.*, vol. 19, no. 11, Nov. 2014, Art. no. 115002.

[13] F. Ayers, A. Grant, D. Kuo, D. J. Cuccia, and A. J. Durkin, "Fabrication and characterization of silicone-based tissue phantoms with tunable optical properties in the visible and near infrared domain," *Proc. SPIE*, vol. 6870, Feb. 2008, Art. no. 687007.

[14] A. M. De Grand *et al.*, "Tissue-like phantoms for near-infrared fluorescence imaging system assessment and the training of surgeons," *J. Biomed. Opt.*, vol. 11, no. 1, 2006, Art. no. 014007.

[15] M. Firbank, M. Oda, and D. T. Delpy, "An improved design for a stable and reproducible phantom material for use in near-infrared spectroscopy and imaging," *Phys. Med. Biol.*, vol. 40, no. 5, pp. 955–961, May 1995.

[16] J. Wang, J. Lin, Y. Chen, C. G. Welle, and T. J. Pfefer, "Phantom-based evaluation of near-infrared intracranial hematoma detector performance," *J. Biomed. Opt.*, vol. 24, no. 4, Apr. 2019, Art. no. 045001.

[17] P. Diep *et al.*, "Three-dimensional printed optical phantoms with customized absorption and scattering properties," *Biomed. Opt. Express*, vol. 6, no. 11, pp. 4212–4220, Nov. 2015.

[18] J. Wang *et al.*, "Three-dimensional printing of tissue phantoms for biophotonic imaging," *Opt. Lett.*, vol. 39, no. 10, pp. 3010–3013, May 2014.

[19] D. M. de Bruin *et al.*, "Optical phantoms of varying geometry based on thin building blocks with controlled optical properties," *J. Biomed. Opt.*, vol. 15, no. 2, 2010, Art. no. 025001.

[20] A. Curatolo, B. F. Kennedy, and D. D. Sampson, "Structured three-dimensional optical phantom for optical coherence tomography," *Opt. Express*, vol. 19, no. 20, pp. 19480–19485, Sep. 2011.

[21] G. Lamouche *et al.*, "Review of tissue simulating phantoms with controllable optical, mechanical and structural properties for use in optical coherence tomography," *Biomed. Opt. Exp.*, vol. 3, no. 6, pp. 1381–1398, Jun. 2012.

[22] R. B. Saager, C. Kondru, K. Au, K. Sry, F. Ayers, and A. J. Durkin, "Multilayer silicone phantoms for the evaluation of quantitative optical techniques in skin imaging," *Proc. SPIE*, vol. 7567, Feb. 2010, Art. no. 756706.

[23] M. S. Wróbel, A. P. Popov, A. V. Bykov, M. Kinnunen, M. Jędrzejewska-Szczerska, and V. V. Tuchin, "Multi-layered tissue head phantoms for noninvasive optical diagnostics," *J. Innov. Opt. Health Sci.*, vol. 8, no. 3, May 2015, Art. no. 1541005.

[24] B. Leh *et al.*, "Optical phantoms with variable properties and geometries for diffuse and fluorescence optical spectroscopy," *J. Biomed. Opt.*, vol. 17, no. 10, Oct. 2012, Art. no. 108001.

[25] M. R. N. Avanaki, A. G. Podoleanu, M. C. Price, S. A. Corr, and S. A. Hojjatoleslami, "Two applications of solid phantoms in performance assessment of optical coherence tomography systems," *Appl. Opt.*, vol. 52, no. 29, pp. 7054–7061, Oct. 2013.

[26] S. Jiang, B. W. Pogue, T. O. McBride, and K. D. Paulsen, "Quantitative analysis of near-infrared tomography: Sensitivity to the tissue-simulating precalibration phantom," *J. Biomed. Opt.*, vol. 8, no. 2, pp. 308–316, Apr. 2003.

[27] C. C. Sthalekar, Y. Miao, and V. J. Koomson, "Optical characterization of tissue phantoms using a silicon integrated fdNIRS system on chip," *IEEE Trans. Biomed. Circuits Syst.*, vol. 11, no. 2, pp. 279–286, Apr. 2017.

[28] X. Intes, J. Yu, A. G. Yodh, and B. Chance, "Development and evaluation of a multi-wavelength multi-channel time resolved optical instrument for NIR/MRI mammography co-registration," in *Proc. IEEE 28th Annu. Northeast Bioeng. Conf.*, Apr. 2002, pp. 91–92.

[29] M. Norgia, A. Pesatori, and L. Rovati, "Optical flowmeter for blood extracorporeal circulators," in *Proc. IEEE Instrum. Meas. Technol. Conf.*, May 2009, pp. 1759–1762.

[30] E. L. Hull, M. G. Nichols, and T. H. Foster, "Quantitative broadband near-infrared spectroscopy of tissue-simulating phantoms containing erythrocytes," *Phys. Med. Biol.*, vol. 43, no. 11, pp. 3381–3404, Nov. 1998.

[31] M. A. Franceschini, D. K. Joseph, T. J. Huppert, S. G. Diamond, and D. A. Boas, "Diffuse optical imaging of the whole head," *J. Biomed. Opt.*, vol. 11, no. 5, 2006, Art. no. 054007.

[32] S. T. Flock, S. L. Jacques, B. C. Wilson, W. M. Star, and M. J. C. van Gemert, "Optical properties of intralipid: A phantom medium for light propagation studies," *Lasers Surg. Med.*, vol. 12, no. 5, pp. 510–519, 1992.

[33] C. D. Kurth, H. Liu, W. S. Thayer, and B. Chance, "A dynamic phantom brain model for near-infrared spectroscopy," *Phys. Med. Biol.*, vol. 40, no. 12, pp. 2079–2092, Dec. 1995.

[34] A. Yodh and B. Chance, "Spectroscopy and imaging with diffusing light," *Phys. Today*, vol. 48, no. 3, pp. 34–40, Mar. 1995.

[35] P. D. Ninni, F. Martelli, and G. Zaccanti, "Intralipid: Towards a diffusive reference standard for optical tissue phantoms," *Phys. Med. Biol.*, vol. 56, no. 2, pp. N21–N28, Jan. 2011.

[36] L. Gagnon, M. Desjardins, J. Jehanne-Lacasse, L. Bherer, and F. Lesage, "Investigation of diffuse correlation spectroscopy in multi-layered media including the human head," *Opt. Express*, vol. 16, no. 20, pp. 15514–15530, Sep. 2008.

[37] A. Gibson *et al.*, "Optical tomography of a realistic neonatal head phantom," *Appl. Opt.*, vol. 42, no. 16, pp. 3109–3116, Jun. 2003.

[38] S. Del Bianco *et al.*, "Liquid phantom for investigating light propagation through layered diffusive media," *Opt. Express*, vol. 12, no. 10, pp. 2102–2111, May 2004.

[39] M. Izzetoglu, S. Malaeb, N. Arora, E. Veznedaroglu, and B. Ben Dor, "Near infrared spectroscopy based non-invasive cerebral edema monitoring system," in *Proc. Soc. fNIRS Conf.*, Paris, France, Oct. 2016, p. 1.

[40] M. Izzetoglu, S. Malaeb, K. Izzetoglu, H. Ayaz, B. Onaral, and B. Ben Dor, "Cerebral edema and oximetry monitoring using NIRS," in *Proc. Britton Chance Symp.*, Philadelphia, PA, USA, Jun. 2018, p. 1.

[41] S. N. Malaeb, M. Izzetoglu, J. McGowan, and M. Delivoria-Papadopoulos, "Noninvasive monitoring of brain edema after hypoxia in newborn piglets," *Pediatric Res.*, vol. 83, no. 2, pp. 484–490, Feb. 2018.

[42] C. S. Robertson *et al.*, "Clinical evaluation of a portable near-infrared device for detection of traumatic intracranial hematomas," *J. Neurotrauma*, vol. 27, no. 9, pp. 1597–1604, Sep. 2010.

[43] R. Salonia, M. J. Bell, P. M. Kochanek, and R. P. Berger, "The utility of near infrared spectroscopy in detecting intracranial hemorrhage in children," *J. Neurotrauma*, vol. 29, no. 6, pp. 1047–1053, Apr. 2012.

[44] J. Leon-Carrion, J. M. Dominguez-Roldan, U. Leon-Dominguez, and F. Murillo-Cabezas, "The Infrascanner, a handheld device for screening *in situ* for the presence of brain haematomas," *Brain Injury*, vol. 24, no. 10, pp. 1193–1201, Sep. 2010.

[45] Z. B. Semenova, A. V. Marshintsev, A. V. Melnikov, S. V. Meshcheryakov, A. R. Adayev, and V. I. Lukyanov, "Infrascanner in the diagnosis of intracranial lesions in children with traumatic brain injuries," *Brain Injury*, vol. 30, no. 1, pp. 18–22, Jan. 2016.

[46] *Wratten 2 Filters*. Accessed: Oct. 28, 2019. [Online]. Available: http://www.kodak.com

[47] R. Bays *et al.*, "Three-dimensional optical phantom and its application in photodynamic therapy," *Lasers Surg. Med.*, vol. 21, no. 3, pp. 227–234, 1997.

[48] G. C. Beck, N. Akgün, A. Rück, and R. Steiner, "Design and characterisation of a tissue phantom system for optical diagnostics," *Lasers Med. Sci.*, vol. 13, no. 3, pp. 160–171, Oct. 1998.

[49] J. Zhang *et al.*, "Application of I&Q detection system in scouting the curative effect of neck squamous cell carcinoma," *Proc. SPIE*, vol. 4955, pp. 575–581, Jul. 2003.

[50] F. B. Haeussinger, S. Heinzel, T. Hahn, M. Schecklmann, A.-C. Ehlis, and A. J. Fallgatter, "Simulation of near-infrared light absorption considering individual head and prefrontal cortex anatomy: Implications for optical neuroimaging," *PLoS ONE*, vol. 6, no. 10, 2011, Art. no. e26377.

[51] M. S. Beauchamp *et al.*, "The developmental trajectory of brain-scalp distance from birth through childhood: Implications for functional neuroimaging," *PLoS ONE*, vol. 6, no. 9, 2011, Art. no. e24981.

[52] Y. Hoshi, M. Shimada, C. Sato, and Y. Iguchi, "Reevaluation of near-infrared light propagation in the adult human head: Implications for functional near-infrared spectroscopy," *J. Biomed. Opt.*, vol. 10, no. 6, 2005, Art. no. 064032.

[53] A. Custo, W. M. Wells, III., A. H. Barnett, E. M. C. Hillman, and D. A. Boas, "Effective scattering coefficient of the cerebral spinal fluid in adult head models for diffuse optical imaging," *Appl. Opt.*, vol. 45, no. 19, pp. 4747–4755, Jul. 2006.

[54] H. Ayaz, M. Izzetoglu, K. Izzetoglu, B. Onaral, and B. Ben Dor, "Early diagnosis of traumatic intracranial hematomas," *J. Biomed. Opt.*, vol. 24, no. 5, Feb. 2019, Art. no. 051411.
[55] J. Choi *et al.*, "Noninvasive determination of the optical properties of adult brain: Near-infrared spectroscopy approach," *J. Biomed. Opt.*, vol. 9, no. 1, pp. 221–230, 2004.
[56] R. B. Burns and C. B. Dobson, "Standard error of the difference between means," in *Experimental Psychology*. Lancaster, U.K.: MTP Press, 1981, pp. 151–157.

Meltem Izzetoglu received the Ph.D. degree in electrical and computer engineering from Drexel University, Philadelphia, PA, USA, in 2002.

She is an Assistant Professor in electrical and computer engineering with Villanova University, Villanova, PA, USA. Her research is centered around design, development, and testing of functional near infrared spectroscopy (fNIRS)-based brain imaging systems using laboratory phantoms, animal models and human experimentation, signal processing and algorithm development for artifact cancelation and information extraction. Her research projects involve the application of fNIRS technology for brain activity and physiological monitoring in everyday and everywhere environments as well as in clinics in all age groups from infants to older adults of healthy and disease populations such as traumatic brain injury and multiple sclerosis patients.

Juan Du received the B.S. degree from the Chongqing University of Civil Engineering and Architecture, Chongqing, China, in 1986, where her special focus was on electro-mechanical device installation.

She is a Research Technician with the School of Biomedical Engineering, Drexel University, Philadelphia, PA, USA. Her research is centered around the design, development, and evaluation of tissue simulating phantoms for optical spectroscopy and imaging applications, device development, calibration, and testing.

Kurtulus Izzetoglu received the Ph.D. degree from the School of Biomedical Engineering, Science and Health Systems, Drexel University, Philadelphia, PA, USA, in 2008.

His research and teaching interests are in functional brain imaging, human performance, learning, training, medical sensor development, biomedical systems, and signal processing. He has background in both electrical and biomedical engineering coupled with the experience of developing and adopting highly portable optical brain imaging systems for the field use in applications ranging from health care to aerospace domain. His current research projects focus on the integration of biosensors for personalized training in safety critical tasks and brain-in-the-loop studies to improve human performance and experience both in clinical and aviation (autonomous systems) settings. He and his students are also interested in research focusing on sensor and algorithm development for sedation monitoring, point-of-care monitoring in prolonged field care, and investigation of biomarkers for evaluation of cerebral vascular reactivity in traumatic brain injury.

Hasan Ayaz (Senior Member, IEEE) is an Associate Professor with the School of Biomedical Engineering Science and Health Systems, Drexel University, Philadelphia, PA, USA. His research involves understanding the neural mechanisms related to human cognitive, and motor functioning with a focus on real-world contexts, utilizing mobile neuroimaging, and deploying neuroengineering approaches for neuroergonomics applications. His research aims to design, develop, and utilize (i.e., to measure $\rightarrow$ elucidate $\rightarrow$ enable) next generation optical brain imaging for neuroergonomic applications over a broad-spectrum including aerospace to health care.

Banu Onaral (Fellow, IEEE) received the Ph.D. degree in bioengineering from the University of Pennsylvania, Philadelphia, PA, USA, in 1978.

She is a H. H. Sun Professor in biomedical and electrical engineering with the School of Biomedical Engineering, Science and Health Systems, Drexel University, Philadelphia, PA, USA. Her academic focus both in research and teaching is centered on information and system engineering with special emphasis on complex systems, biomedical signal processing in ultrasound and functional optical brain imaging. She is the founder of several research laboratories including the Cognitive Neuroengineering and Quantitative Experimental Research (CONQUER) CollabOrative.

Dr. Onaral founded the School of Biomedical Engineering, Science and Health Systems and served as the Founding Dean (1997–2014). In this capacity, she led the translational research initiative for rapid commercialization of biomedical technologies developed at Drexel University. The program has been awarded the Coulter-Drexel Translational Research Partnership Endowment. She is a fellow of the American Association for the Advancement of Science (AAAS) and a Founding Fellow of American Institute for Medical and Biological Engineering (AIMBE). She is currently serves as the Senior Presidential Advisor for "Global Innovation Partnerships" at Drexel University and leads the development of the Global Innovation Partnership endowment created under her name. Throughout her career, she actively forged international academic and translational research partnerships with universities as well as science and technoparks, primarily in China and Turkey.

Baruch Ben Dor is a graduate of Talpiot Program with the Israeli Air Force, Tel Aviv, Israel, and received the Ph.D. degree in physics from Technion, Haifa, Israel, in 1996.

He is the Chief Executive Officer (CEO) of InfraScan, Philadelphia, PA, USA. He created InfraScan, a medical device company focused on handheld systems for detection of brain hematomas. He developed the company business plan, raised over $16.5M, got DeNovo FDA clearance, and launched sales. All battalion aid stations of the US Marines are equipped with the Infrascanner, saving lives.